



TECHNICAL ARTICLE

Fabrication and Fatigue Properties of Dissimilar Steel Functionally Graded Material Structure Through Wire Arc Additive Manufacturing

Yusuf Ayan and Nizamettin Kahraman

Submitted: 8 August 2022 / Revised: 1 October 2022 / Accepted: 19 January 2023 / Published online: 17 February 2023

Functionally graded materials (FGM) are structures that can provide different material properties together. To produce these structures, the additive manufacturing method has been used and preferred. In this study, an FGM structure was fabricated by wire arc additive manufacturing (WAAM) process using low-alloy ER70S-6 and austenitic stainless steel 308LSi metal wires. The FGM structure was characterized by tensile, fatigue, hardness tests, and microstructure examinations. As a result of the applied tests, it was found that the FGM structure has strong interfacial strength. In addition, no formations or defects that could reduce the strength of the FGM part were observed at the interface and in the regions close to the interface. The sides of the FGM part containing the base material could reflect their characteristic material properties. FGM part, whose properties can be changed partially, has been successfully fabricated.

Keywords dissimilar, fatigue, FGM, functionally graded materials, steel, WAAM, wire arc additive manufacturing

1. Introduction

Depending on the advancement of technology in today's industry, there is a need for components that provide different material properties locally as a single structure. Functionally graded materials (FGM) have emerged as an advanced type of material to manufacture these components. These are generally preferred for critical and crucial service conditions, thanks to providing different material properties within the same construction (Ref 1). In addition, performing FGM fabrication with two metals can provide cost reduction instead of using a single high-cost material for the entire part (Ref 2). The manufacturing of FGM structures by traditional methods is often complicated. These structures, which can contain two metals, can be fabricated using the additive manufacturing (AM) technique (Ref 3). AM technologies offer an exclusive, cost-effective capability to manufacture hybrid or multi-material parts for superior performance (Ref 4). AM technique has the advantage, especially in manufacturing complex-shaped FGM structures. The application of the AM method with layer control has made it possible to use different materials in the desired layer.

Today, different methods have been developed for the AM process of metals. The most common metal additive manufacturing techniques are selective laser melting (SLM), electron

beam melting (EBM), and wire arc additive manufacturing (WAAM) (Ref 5). In the WAAM method, a welding arc is used as a heat source, and wire is used as raw material (Ref 6). This method allows the economical production of large-scale and high-density parts (Ref 7). WAAM enables the fabrication of custom geometries through direct fabrication from 3D data and hybrid fabrication, functionally graded materials, and manufacturing of integrated functionality parts (Ref 8). Since the welding arc is used to melt the metal wire in the WAAM process, many metal types can be processed with high arc temperatures from low to high melting points. Thanks to these advantages, WAAM has a valuable spot in fabrication of FGM structure. In the previous study, for the definition of qualified part fabrication by the WAAM, the terms, functionally graded materials (FGM) (Ref 9), bimetal (Ref 2), dissimilar alloys (Ref 10), and multi-materials (Ref 11), are used.

Previous studies on the fabrication of FGM parts with WAAM mostly adopted two different procedures. The first of these is to fabricate layers by using two different wire materials simultaneously. In this method, the chemical content of the built layer can be adjusted as desired by changing the feeding speed of the wires. In this way, alloying can be made, or structures containing intermetallics can be created intentionally. In the second procedure, a material was generally used up to a specific layer region, and the FGM structure was manufactured by changing the material in other layers. Thus, this structure consists of areas containing two different material sides with different properties. As an example of these studies, Singh et al. (Ref 12) fabricated an FGM structure with NiTi and 316L wires. They stated that both materials were generally dendritic in microstructure, and intermetallics of TiCr₂, FeNi, NiTi, TiNi₃, and TiNi₂ were formed at the interface. Shen et al. (Ref 13) manufactured Fe-Fe₃Ni FGM structure by simultaneously applying two different Fe- and Ni-based wire feeding in the TIG-WAAM process. The authors stated that the Fe-Ni binary system has unique physical properties, and the FGM structure has full density and smooth composition transitions. Wang et al.

Yusuf Ayan, Mechatronics Engineering, Karabuk University, Karabük, Türkiye; and **Nizamettin Kahraman**, Manufacturing Engineering, Karabuk University, Karabük, Türkiye. Contact e-mail: yusufayan@karabuk.edu.tr.

(Ref 14) emphasized that TiAl alloys have strong mechanical properties and fabricated titanium aluminide FGM by TIG welding with pure titanium and pure aluminum wires. Tian et al. (Ref 10) applied the fabrication of FGM structure, consisting of Ti on one side and Al-based material on the other, using the CMT-WAAM method. The constructions were involved in two ways: Ti then Al and Al then Ti. They obtained better tensile strength in the first fabrication, and the intermetallic types that occurred at the interface varied according to the material used as a priority in the fabrication. They observed brazing joint formation in the structure where Ti was produced before and fusion joint formation in the other. Chandrasekaran et al. (Ref 15) performed an FGM fabrication by WAAM method using ER70S-6 carbon–manganese and ER2209 duplex stainless steel wires. They obtained a strong interface in the FGM structure and maintained that it could be used instead of the so-called marine riser used to extract crude oil in the marine industry. Kannan et al. (Ref 16) used SS904L and Hastelloy C-276 metal wires to fabricate FGM structure by the gas metal arc welding (GMAW) method. They obtained a strong bimetallic interface in the FGM structure, and no defects were found.

As mentioned in the previous paragraph, there have been many studies on FGM production with WAAM. These have generally been carried out lately due to the recent adoption of AM technology. In this study, FGM fabrication was carried out

with low-alloy steel ER70S-6 and austenitic stainless steel 308LSi wires, which are widely used in the industry, by the WAAM method. One of the different aspects of the study was the determination of the fatigue strength of the steel FGM structure, which was rarely applied in the previous studies. Considering that most of the damage in metals is caused by fatigue (Ref 17), it is essential to know the fatigue strength of FGM structures manufactured through WAAM. In addition, the presented study investigated the properties of the steel FGM structure by applying other mechanical and metallurgical tests.

2. Materials and Methods

Two steel wire materials, ER70S-6 and 308LSi, with 1.2 mm diameters, were used to fabricate the FGM part. The wires were deposited on the St-37 plate with a dimension of $20 \times 150 \times 400$ mm. The chemical compositions of the wire and substrate materials are given in Table 1. In the manufacturing processes, a customized machine was used in which the worktable can rotate 360° on its own axis, the angle of the torch can be changed relative to the workpiece and the torch can move in three axes. A GMAW welding unit was added to this machine, and the manufacturing process was carried out with this method. The FGM fabrication principle is shown in Fig. 1. Fabrication parameters are given in Table 2. The first 24 of the total layers of the produced FGM part consist of ER70S-6, and the other 18 are 308LSi. After each layer was built, it was waited to cool down to $90\text{--}100^\circ\text{C}$, and the next layer was fabricated following the cooling. The manufactured FGM part is shown in Fig. 2(a). The part was fabricated as a single track with approximate dimensions of 315 mm length, 80 mm width and 132 mm height. The average layer thickness was measured as 8 mm, as result of the measurements taken from different

Table 1 Main chemical contents of feeding wires and substrate (weight %)

	C	Si	Mn	Cr	Ni	Fe
ER70S-6	0.07	0.9	1.45	Rest
308LSi	0.01	0.7	1.9	20	9.5	Rest
St-37	0.17	0.3	1.4	Rest

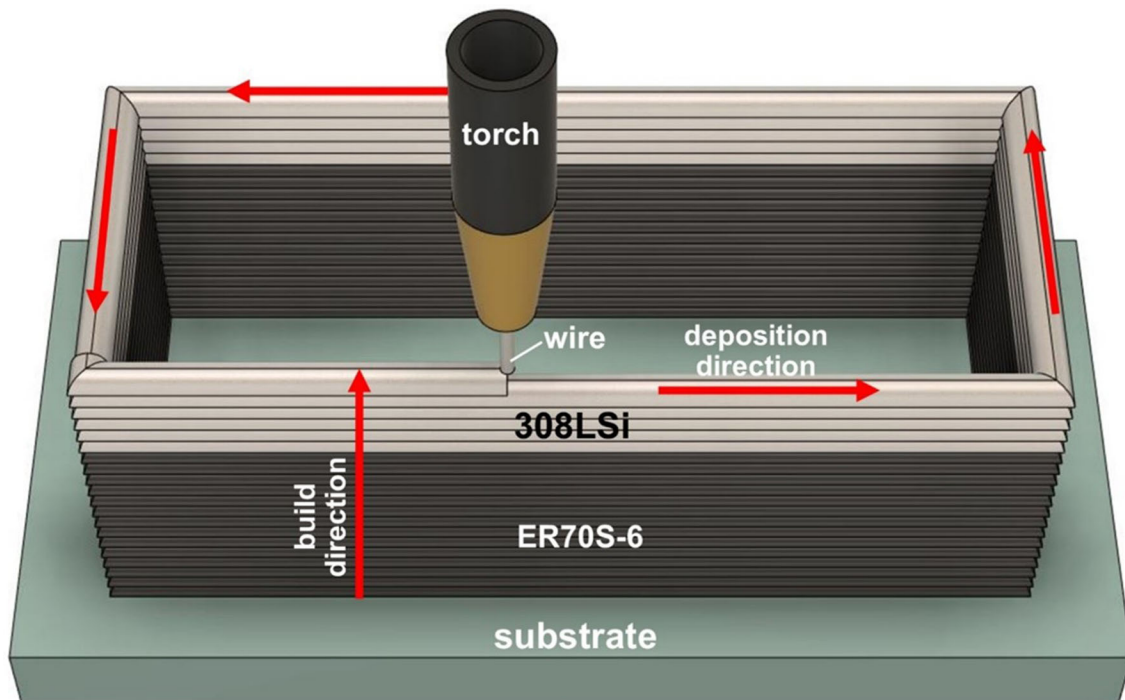


Fig. 1 WAAM material deposition principle

Table 2 WAAM process parameters

	ER70S-6	308LSi
Current, A	105-120	100-125
Voltage, V	17-19	18-20
Wire feed rate, m/min	2	3
Travel speed, mm/min	150	150
Shielding gas	86% Ar + 12% CO ₂ + 2% O ₂	98% Ar + 2% CO ₂
Shielding gas flow rate, L/min	15	15

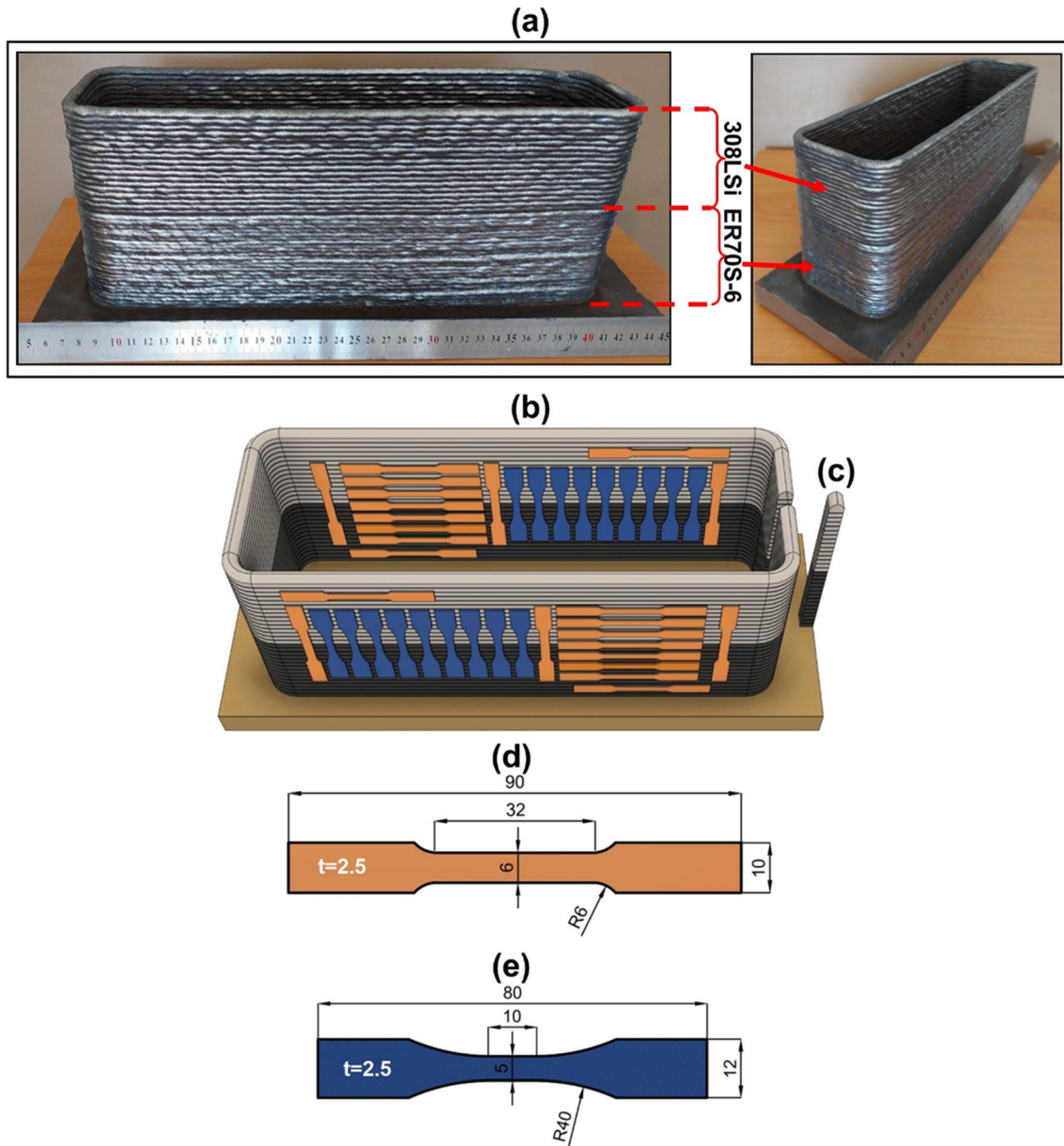


Fig. 2 (a) Fabricated FGM part, (b) test sample locations, (c) microhardness- microstructure sample, (d) tensile, and (e) fatigue test specimen dimensions

points of the FGM part. Tensile, fatigue, and hardness tests were applied to the FGM part. In addition, XRD analyses and microstructure studies were carried out with an optical micro-

scope. The part first was milled to 2.5 mm thickness for the tensile and fatigue tests.

In Fig. 2(b), the location of the test samples extracted from the FGM part is illustrated. The dimensions of the test

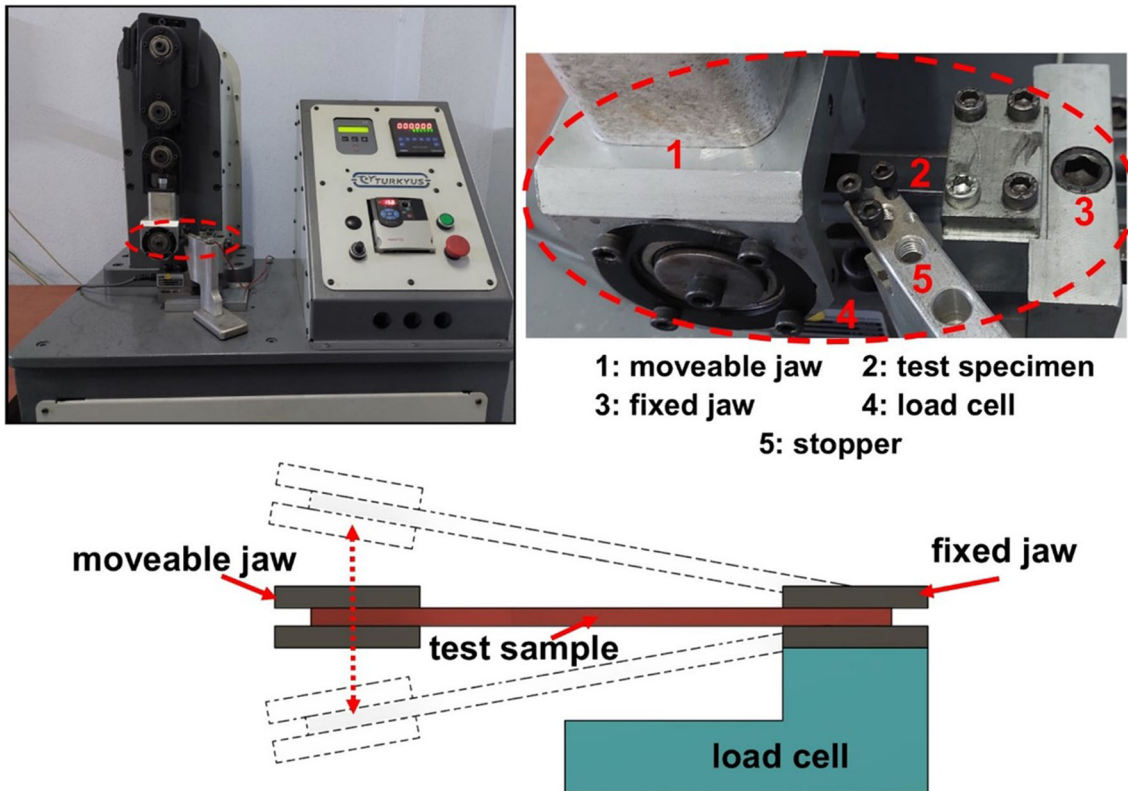


Fig. 3 Fatigue test machine, its components, and the test principle

specimens are shown in Fig. 2(d) and (e). Tensile tests were carried out with a 50 kN capacity Shimadzu test machine. The tests were carried out at room temperature and at a cross-head speed of 2 mm/min. Six samples were taken from the build direction (vertical) and 18 samples from the deposition direction (horizontal) of the FGM part. Horizontal samples were taken from the ER70S-6, 308LSi sides, and the interface region of these two materials. After the tensile test, fracture surface examinations were carried out by SEM (scanning electron microscope).

Fatigue tests were performed with a customized test machine applying bending stress. In total, 36 samples taken from the vertical and horizontal direction of the FGM part were subjected to the test. The tests were applied at six different stress amplitudes, using three samples for each amplitude. In addition, the test was applied up to 10^7 cycles at the lowest stress value. The test speed was chosen as 10 Hz. The machine used in the tests and the test method is shown in Fig. 3. The fractured surface of one of the test specimens damaged after the fatigue was examined by SEM.

Vickers method was used for microhardness tests. In the tests, 500 g load was applied, and the dwell time was set to 10 s. Hardness measurements were made on the sample obtained as a cross section of the FGM part, as shown in Fig. 2(c). Measurements were taken at equal intervals up to the interface for both material sides along the build direction. The same sample tested in microhardness was used for microstructure examinations. 4% nital solution was used for etching the ER70S-6 side of the microstructure sample with a dwell time 10 s. On the 308LSi side, electrolytic etching method was used, and the sample was etched in 10% oxalic acid solution for 60 s with 15 s periods. The interface of the FGM part and the

microstructure of the base material sides close to the interface were examined with a Nikon Epiphot 200 optical microscope. In XRD studies, the phase characteristics of the interface and the main material sides close to the interface were investigated.

3. Results and Discussions

3.1 Tensile Test

Figure 4(a, vertical and b, horizontal) shows the condition of the FGM specimens after the tensile test. Stress–strain plots obtained from the tensile test machine are shown in Fig. 4(c), (d), (e), and (f). Due to a large number of samples, only tensile graphs of certain samples are given for horizontal orientation. The evaluation of the tensile test results was started by examining the fracture conditions at the macroscale. When the macrofracture images of vertical specimens are examined as in Fig. 4(a), it is seen that all specimens were fractured from the ER70S-6 side. In this case, it can be said that the strength of the interface, which consists basically of low alloy steel and stainless steel, is higher than ER70S-6 side. In addition, it can be stated that there is no defect in the interface of the FGM part that will reduce the strength, and a strong interface is formed in terms of joining. In addition, the fractures that occur far from the interface is another positive result. In other words, there was no tensile rupture due to tensile stress both at the interface and in the regions close to the interface. Thus, it is understood that there are no faults caused by joining on the sides close to the interface and that the strength of these sides is close to or higher than the ER70S-6 base material. All these conditions make the FGM part successful in terms of tensile strength.

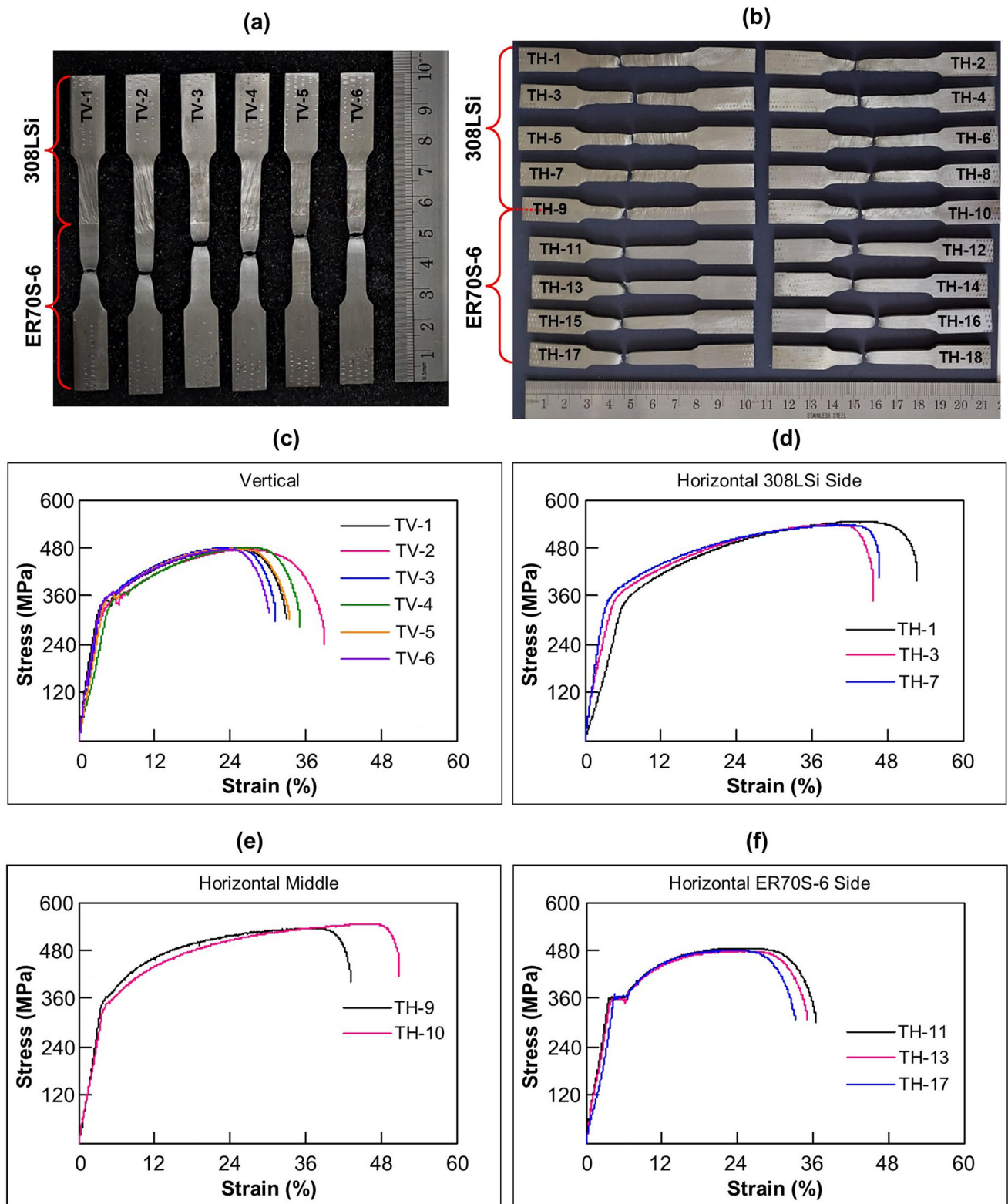


Fig. 4 Tensile test specimens after the test (a) vertical, (b) horizontal, stress–strain plots: (c) vertical, (d) horizontal (308LSi side), (e) horizontal (middle), and (f) horizontal (ER70S-6 side)

The mean tensile strength of the vertical samples was calculated as 482 MPa, and the maximum elongation value was 25%. Considering that these samples fractured on the ER70S-6 side, it should be expected that their tensile strength is close to the tensile strength of the WAAM structure produced with only

ER70S-6 wire. Previous studies show that the tensile strength of WAAM structures manufactured with ER70S-6 generally varies between 470 and 500 MPa (Ref 18–21). Since these values are very close to the vertical samples of the FGM part

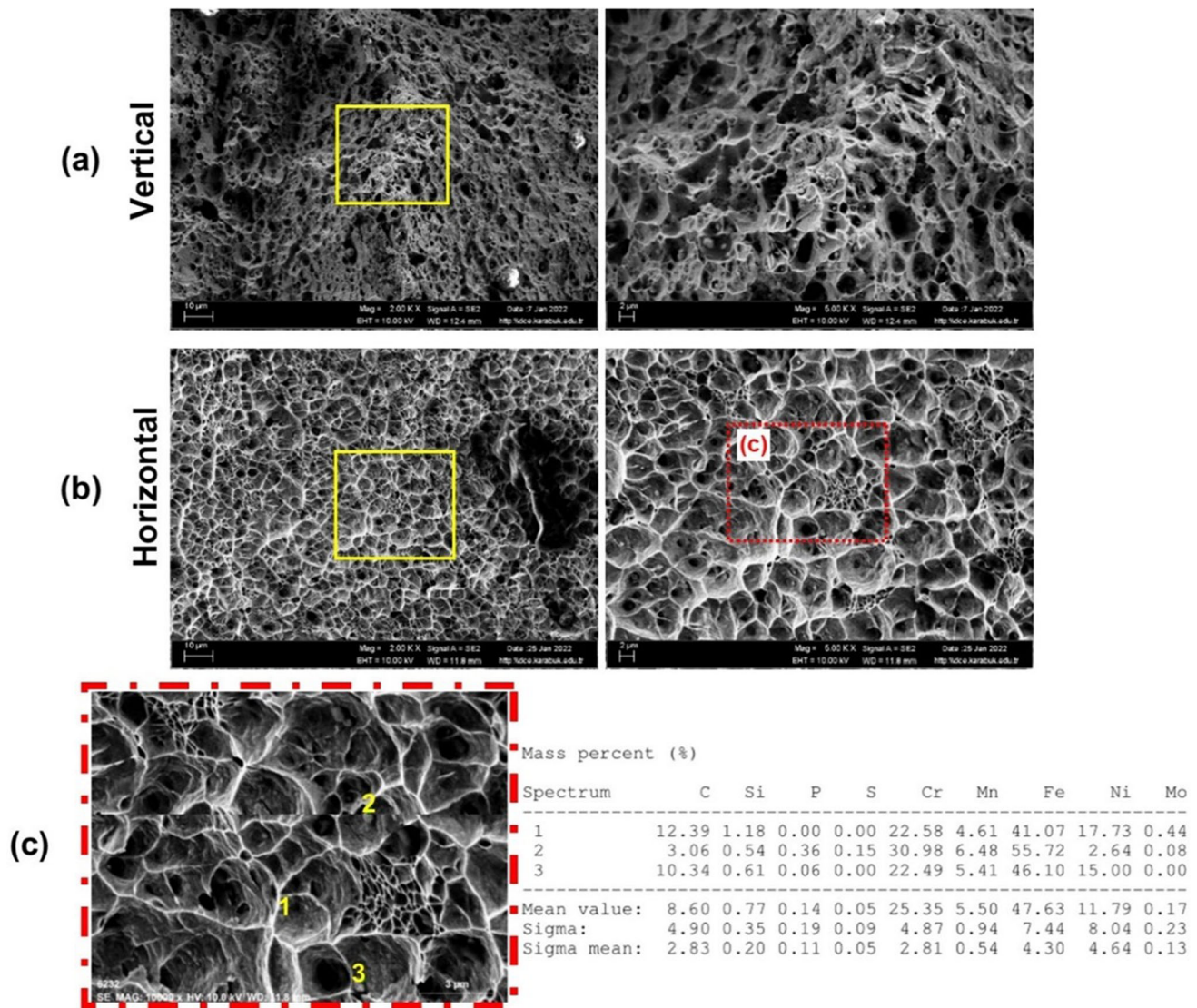


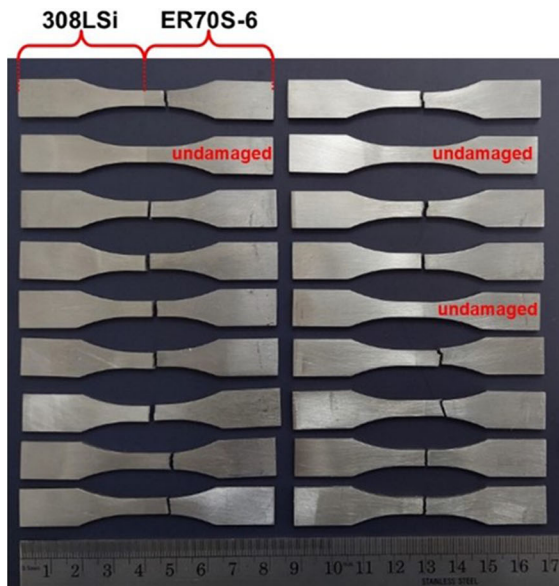
Fig. 5 Fracture surfaces of the tensile test specimens (a) vertical, (b) horizontal, and (c) square in b and EDS results

fabricated in the study, the ER70S-6 side of the FGM structure reflected its own characteristics in terms of tensile strength.

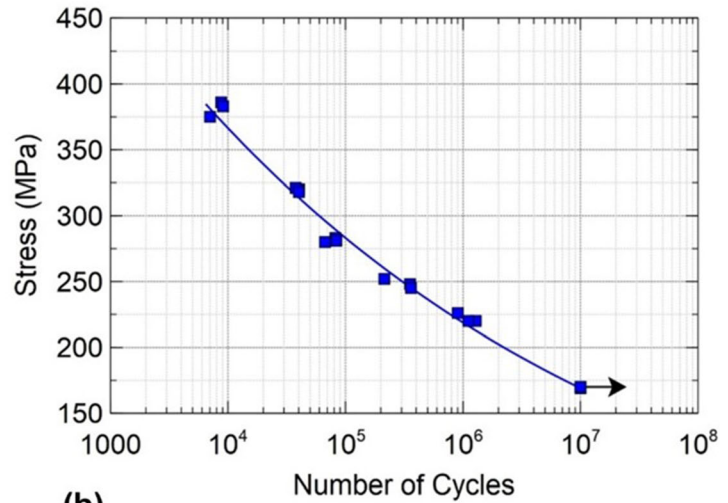
Horizontal tensile test specimens have a uniform material content up to the interface region of the FGM part. Apart from these, horizontal samples of TH-9 and TH-10, which are nearly equidistant from the interface of both materials, contain an extended joint interface along the tensile axis. The mean tensile strength of the samples, all containing 308LSi material, was found to be 532 MPa, and the maximum elongation value was 42%. Gordon et al. (Ref 22) evaluated tensile strength of 524 ± 13 MPa in the horizontal direction in the WAAM part produced with 308L wire. This value is very close to the 308LSi side of the FGM structure. In this case, it can be said that the 308LSi side of the FGM structure reflects the main material properties in terms of tensile strength. The average tensile strength of the samples located in the horizontal middle region of the FGM part and containing a long interface along the tensile axis was calculated as 544 MPa, and the maximum elongation was 41.7%. These are very close to the 308LSi side of the FGM part. On the ER70S-6 side of the horizontal samples, 484 MPa tensile strength and 23.6% maximum elongation were calculated. This is quite close to what is found

in the literature, as described in the previous paragraph. When the tensile strength of the FGM structure is evaluated in general, it is understood that the parts containing the base material reflect their own characteristics, and the interface strength of the FGM part is high. Besides, it can be emphasized that no detrimental formations that can reduce the tensile strength occur at the interface and near the interface of the FGM structure.

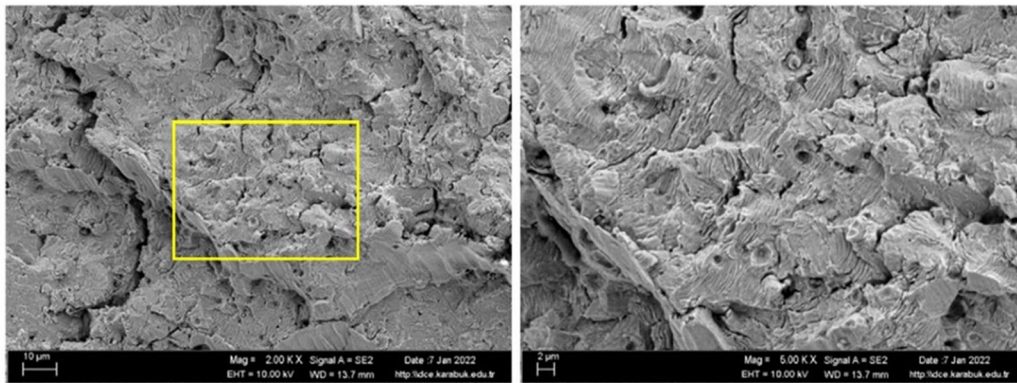
The fracture surface images of the tensile test specimens examined by SEM shown in Fig. 5. Different sized dimples are observed in the surface texture. It is seen that the dimples are smaller and more numerous in the horizontal sample. This also indicates that the ductility of the horizontal sample is higher. However, both samples showed ductile fracture behavior according to their dimples states. Inclusions of varying sizes were observed in vertical and horizontal fracture's surface images. It was observed that the inclusion distribution varied locally but concentrated in the main regions where the fracture occurred. When the previous studies were examined, similar inclusion structures were identified as MnO (Manganeseoxide) (Ref 23–25). Oxidizing ability of the shielding gas and the high heat input and rapid cooling in WAAM process could be the



(a)



(b)



(c)

Fig. 6 (a) Samples after fatigue test, (b) fatigue test S-N plot, and (c) fracture surface of the test specimen

reasons of formation of MnO (Ref 26). Considering the EDS results in Fig. 5(c), it is understood that inclusions or secondary phases may be found on the fractured surface.

3.2 Fatigue Test

The first evaluation of the fatigue specimens was performed by examining the fracture regions on the macroscale since they contain an interface. Figure 6(a) shows the fracture condition of the fatigue test specimens after the test. All of the fatigue test samples were fractured from the ER70S-6 side. Thus, based on the WAAM fabrication parameters applied to the FGM part, it could be stated that there is no defect at the interface that reduces the fatigue strength.

The fatigue graph obtained from the fatigue tests is given in Fig. 6(b). The fatigue life of 8.3×10^3 was reached in the low-cycle fatigue region with the highest stress of 385 MPa applied in the fatigue tests. The high-cycle fatigue zone was passed at average stress of 245 MPa, where the fatigue life was approximately 3.1×10^5 . The fatigue life of 10^6 was reached at a stress amplitude of about 220 MPa. Experiments were stopped at 10^7 cycles without fatigue damage, and the fatigue limit was calculated as 170 MPa on average. Bartsch et al. (Ref 27) applied the fatigue test to the structure consisting of ER70S-6

manufactured by the WAAM and obtained approximately 3.6×10^6 cycles at a stress value of 190 MPa and stopped the test. Considering that the fatigue strength of the FGM part is about 170 MPa at 10^7 cycles, very close values were acquired with the previous study. In another study, Ron et al. (Ref 28) employed a fatigue test at 50 Hz to the samples obtained from ER70S-6 and St-37 material. They found the fatigue limit of the ER70S-6 structure to be 220 MPa and St-37 to be 230 MPa at 10^8 cycles. Compared to these results, there is a difference of about 50 MPa in the fatigue strength of the FGM part. This difference is thought to be because the fatigue test speed applied in the experiments is five times greater. Guenneq et al. (Ref 29) studied the effects of fatigue test speed (frequency) of low carbon steel and observed that fatigue strength tended to increase with increasing test speed. Zainulabdeen (Ref 30) found the fatigue strength of St-37 material as 160 MPa at 10^6 cycles. According to these, it can be said that the fatigue strength of the FGM structure is not behind the St-37 material which is similar to the chemical content of ER70S-6. Figure 6(c) shows the fracture surfaces of the fatigue specimen examined by SEM. Fatigue crack is seen on this surface. It was determined that the inclusions were less than the tensile test specimens. As a result of fatigue, the fracture behavior was brittle.

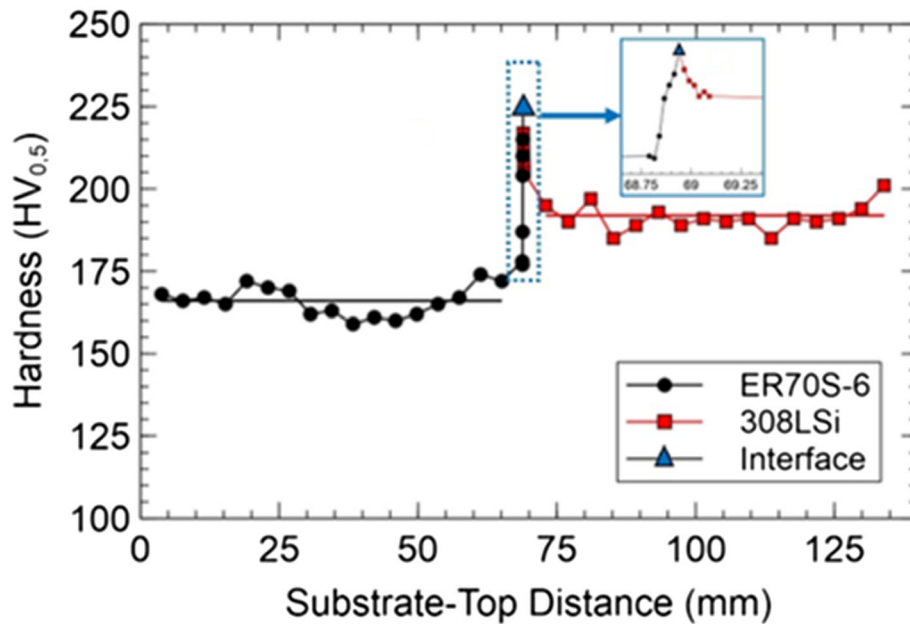


Fig. 7 Microhardness test results

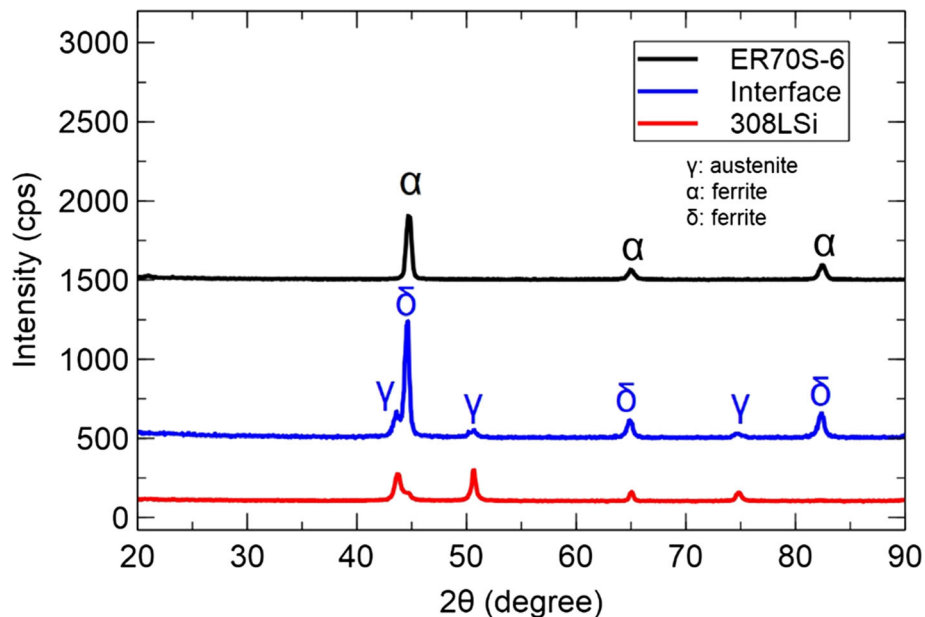


Fig. 8 XRD results of FGM part

3.3 Microhardness

The graph obtained from the hardness values measured along the cross section of the FGM part is shown in Fig. 7. Since the FGM part was produced with two different material combinations, the hardness was evaluated for three different regions. Values in the chart that color it in black identify the ER70S-6 side, and the reds identify the 308LSi side. The average hardness of the ER70S-6 side was calculated as 166 HV. This is very close to the calculated mean hardness values (160 HV) of the WAAM structure produced only with ER70S-6 in previous study (Ref 19). In this respect, the ER70S-6 side of the FGM part provided the main material properties in terms of hardness properties. The mean hardness of the 308LSi layers of

the FGM part was calculated as 191 HV. It is very close to the hardness (about 190–200 HV (Ref 31)) measured in a previous study on a WAAM structure manufactured with only 308L wire. In this case, it can be said that the hardness of the stainless steel side of the FGM part also reflects the main material properties.

When the graph in Fig. 7 is analyzed, the most dramatic situation is the high hardness of the interface. The interface hardness was measured as 225 HV, higher than both main materials. One of the reasons for the interface's high hardness could be the formation of the secondary phase. According to the manufacturer's catalogue data, the high C value on the ER70S-6 side and the high Cr content of 308LSi stainless steel increase the possibility of forming C-containing compounds on

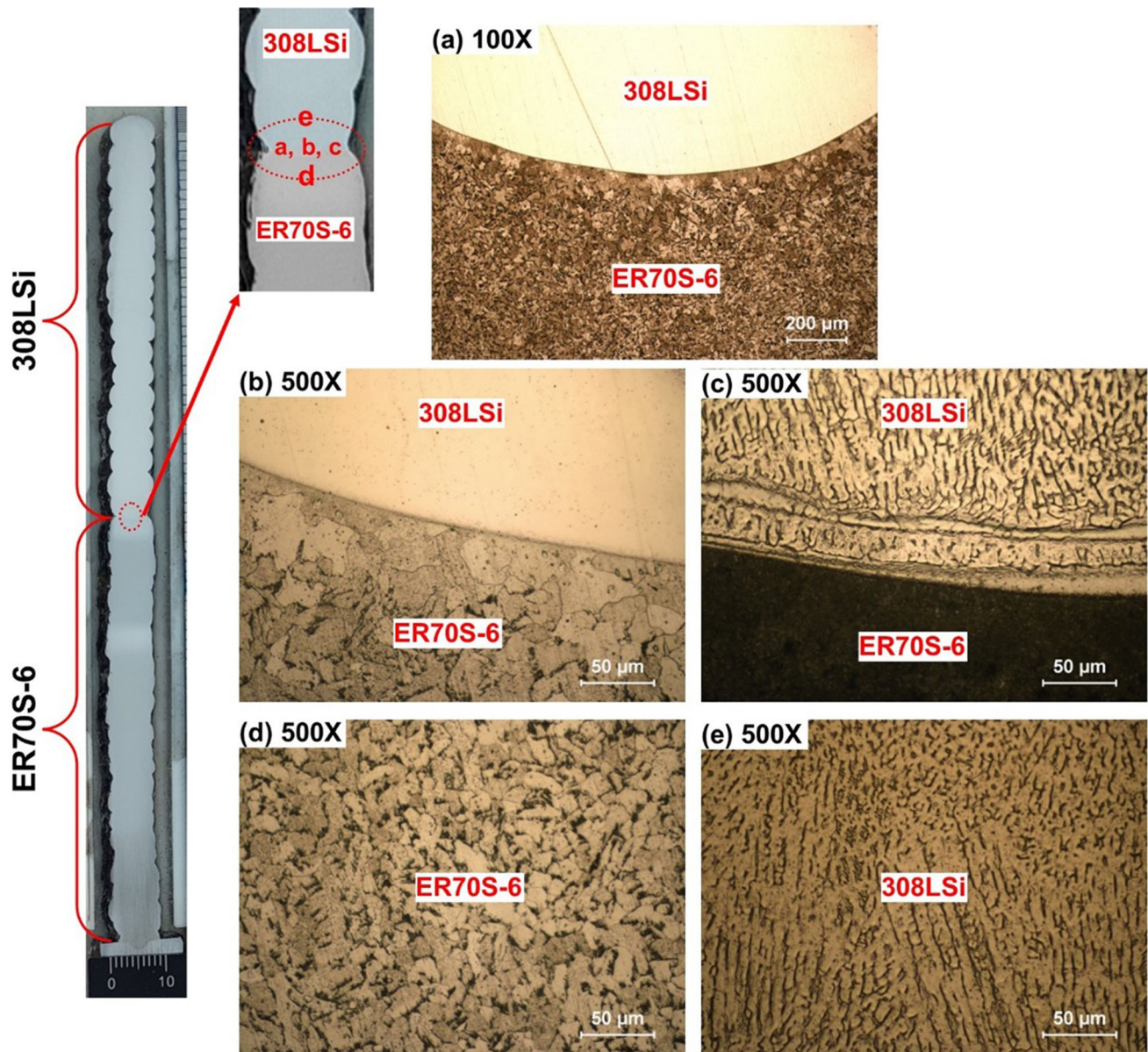


Fig. 9 Microstructure images of FGM part (a) 100X magnification of interface region, (b) interface region without etched 308LSi, (c) interface region, (d) ER70S-6 side, and (e) 308LSi side

the interface. Phases with high chromium content increase the hardness (Ref 32). The transition of the C element to the medium containing a high amount of Cr, which is suitable for carbide formation, causes the progress of martensite at the melting boundary and increases the hardness in the near parts of the grain boundaries (Ref 33). In another study where the interface hardness was high, this increase was attributed to the occurrence of martensitic transformation (Ref 15).

3.4 XRD and Microstructure Examinations

Figure 8 shows the XRD analysis results of the ER70S-6 side near the interface the interface region and the 308LSi side near the interface of the FGM part. It is seen that the resulting peaks of the base materials (ER70S-6 and 308LSi) occur in the main microstructure phases. In this case, in the initial evaluation of the XRD results, it was concluded that the base material regions of the FGM part exhibited their own

microstructure characteristics. In XRD analysis, the interface measurement region covers an area of approximately 2 mm^2 , which includes the interface and the base material sides close to the interface. It is seen that XRD results of the interface shown in blue in the graph in the Fig. 8 is different from the base materials. According to the results, δ ferrite density was higher than γ at the interface and near the interface. While the peaks show the γ phase more intensely in the 308LSi material, this situation changed at the interface, and the peaks were found higher in the δ ferrite phase. Then, it can be mentioned that the interface region of the FGM part has a structure that contains an austenite phase but contains a high percentage of ferrite.

In Fig. 9, the microstructure images taken from the interface of the joint, which has the FGM and the base material regions close to the interface are given. Figure 9(a), (b), and (c) shows the region including the interface, d, the side containing the ER70S-6 near the interface, and e, the 308LSi side near the

interface. The region containing the interface is shown at different magnifications, with the 308LSi material before etching and after etching. In these images, the interface is seen as a line. A large-grained structure was formed in the ER70S-6 part close to the interface. The 308LSi stainless steel part consists of a dendritic structure oriented toward temperature gradients along the build direction. Skeletal and lathy ferrite phases are also observed in this structure. When the microstructure of the ER70S-6 side, which is close to the interface, is examined in Fig. 9(d), a structure containing high polygonal ferrite with pearlite at the grain boundaries is seen. There is also a relatively low amount of acicular ferrite in the structure. Figure 9(e) shows the microstructure of the 308LSi side, which does not include the interface. The structure generally consists of a phase containing high skeletal ferrite in the γ matrix. The dendrites are oriented toward the build direction where the temperature gradients occurred.

4. Conclusions

The following conclusions were drawn in this study, in which the FGM part was produced using the WAAM method with two different steels.

- In the tensile tests, the vertical specimens fractured inside the ER70S-6 side. The main material sides exhibited their own strength properties in the horizontal samples. The tensile strength of the horizontal samples with an extended interface along the tensile axis was close to that of stainless steel.
- Fatigue damage occurred on the ER70S-6 side, and the fatigue strength was calculated as 170 MPa at 10^7 fatigue life.
- As a result of the hardness measurements, the hardness of the interface was found to be the highest. The parts containing the base material exhibited their own hardness characteristics.
- The interface was found to be ferritic in XRD analysis. The ER70S-6 side consists of a polygonal ferritic structure, and the 308LSi side consists of a structure containing δ ferrite in the austenite matrix.
- According to all the tests applied, the FGM part's interface strength was high, and no structure formation that would decrease the tensile and fatigue strength was found in and near the interface region.
- Within the procedure used in the study and the selected WAAM fabrication parameters, a successful FGM structure whose properties can vary regionally could be produced.

Acknowledgments

This work was supported by Karabük University Scientific Research Projects Coordination Unit (Project number: FDK-2019-2130) and the Scientific and Technological Research Council of Turkey (Project number: 219M111). The authors would like to thank these institutions.

Conflict of interest

The authors reported no potential conflict of interest.

References

1. G. Marinelli, F. Martina, H. Lewtas, D. Hancock, S. Ganguly, and S. Williams, Functionally Graded Structures of Refractory Metals by Wire Arc Additive Manufacturing, *Sci. Technol. Weld. Join.*, 2019, **24**, p 495–503. <https://doi.org/10.1080/13621718.2019.1586162>
2. A. Kumar and K. Maji, Microstructure and Chemical Composition Analysis of Double Wire Arc Additive Manufactured Bimetallic Structure, *J. Mater. Eng. Perform.*, 2021, **30**, p 5413–5425. <https://doi.org/10.1007/s11665-021-05819-9>
3. Y. Tian, J. Shen, S. Hu, X. Chen, Y. Cai, and J. Han, Effect of Deposition Layer on Microstructure of Ti–Al Bimetallic Structures Fabricated by Wire and Arc Additive Manufacturing, *Sci. Technol. Weld. Join.*, 2021, **2**, p 1–11. <https://doi.org/10.1080/13621718.2021.1996850>
4. C. Dharmendra, S. Shakerin, and M. Mohammadi, Metallurgical Assessment of Additive Manufactured Nickel Aluminum Bronze-316L Stainless Steel Bimetallic Structure: Effect of Deposit Geometry on the Interfacial Characteristics and Cracking, *J. Mater. Eng. Perform.*, 2021 <https://doi.org/10.1007/s11665-021-06194-1>
5. Y. Zhang, F. Cheng, and S. Wu, Improvement of Pitting Corrosion Resistance of wire arc Additive Manufactured Duplex Stainless Steel Through Post-Manufacturing Heat-Treatment, *Mater. Characterizat.*, 2021, **171**, p 110743. <https://doi.org/10.1016/j.matchar.2020.110743>
6. S.W. Williams, F. Martina, A.C. Addison, J. Ding, G. Pardal, and P. Colegrove, Wire + Arc Additive Manufacturing, *Mater. Sci. Technol.*, 2016, **32**, p 641–647. <https://doi.org/10.1179/1743284715Y.0000000073>
7. A.S. Yildiz, K. Davut, B. Koc, and O. Yilmaz, Wire Arc Additive Manufacturing of High-Strength Low Alloy Steels: Study of Process Parameters and Their Influence on the Bead Geometry and Mechanical Characteristics, *Int. J. Adv. Manuf. Technol.*, 2020, **108**, p 3391–3404. <https://doi.org/10.1007/s00170-020-05482-9>
8. D. Jafari, T.H.J. Vaneker, and I. Gibson, Wire and Arc Additive Manufacturing: Opportunities and Challenges to Control the Quality and Accuracy of Manufactured Parts, *Mater. Des.*, 2021, **202**, p 109471. <https://doi.org/10.1016/j.matdes.2021.109471>
9. S. Mohan Kumar, A. Rajesh Kannan, N. Pravin Kumar, R. Pramod, N. Siva Shanmugam, A.S. Vishnu et al., Microstructural Features and Mechanical Integrity of Wire Arc Additive Manufactured SS321/Inconel 625 Functionally Gradient Material, *J. Mater. Eng. Perform.*, 2021, **30**, p 5692–5703. <https://doi.org/10.1007/s11665-021-05617-3>
10. Y. Tian, J. Shen, S. Hu, J. Gou, and E. Kannatey-Asibu, Wire and arc Additive Manufactured Ti–6Al–4V/Al–6.25Cu Dissimilar Alloys by CMT-Welding: Effect of Deposition Order on Reaction Layer, *Sci. Technol. Weld. Join.*, 2020, **25**, p 73–80. <https://doi.org/10.1080/13621718.2019.1629379>
11. K. Treutler, S. Kamper, M. Leicher, T. Bick, and V. Wesling, Multi-Material Design in Welding Arc Additive Manufacturing, *Metals*, 2019, **9**, p 809. <https://doi.org/10.3390/met9070809>
12. S. Singh, A.N. Jinoop, I.A. Palani, C.P. Paul, K.P. Tomar, and K.G. Prashanth, Microstructure and Mechanical Properties of NiTi-SS Bimetallic Structures Built Using Wire Arc Additive Manufacturing, *Mater. Lett.*, 2021, **303**, p 130499. <https://doi.org/10.1016/j.matlet.2021.130499>
13. C. Shen, X. Hua, M. Reid, K.-D. Liss, G. Mou, Z. Pan et al., Thermal Induced Phase Evolution of Fe–Fe₃Ni Functionally Graded Material Fabricated Using the Wire-Arc Additive Manufacturing Process: An In-situ Neutron Diffraction Study, *J. Alloys Comp.*, 2020, **826**, p 154097. <https://doi.org/10.1016/j.jallcom.2020.154097>
14. J. Wang, Z. Pan, Y. Ma, Y. Lu, C. Shen, D. Cuiuri et al., Characterization of Wire Arc Additively Manufactured Titanium Aluminide Functionally Graded Material: Microstructure, Mechanical Properties and Oxidation Behaviour, *Mater. Sci. Eng., A*, 2018, **734**, p 110–119. <https://doi.org/10.1016/j.msea.2018.07.097>

15. S. Chandrasekaran, S. Hari, and M. Amirthalingam, Wire Arc Additive Manufacturing of Functionally Graded Material for Marine Risers, *Mater. Sci. Eng. A.*, 2020, **792**, p 139530. <https://doi.org/10.1016/j.msea.2020.139530>
16. A. Rajesh Kannan, S. Mohan Kumar, R. Pramod, N. Pravin Kumar, N. Siva Shanmugam, and Y. Palguna, Microstructure and Mechanical Properties of Wire Arc Additive Manufactured bi-Metallic Structure, *Sci. Technol. Weld. Joining*, 2021, **26**, p 47–57. <https://doi.org/10.1080/13621718.2020.1833140>
17. W.D. Callister, D.D. Rethwisch, K. Genel, C. Bindal, M. Demirkol, R. Artır et al., Malzeme Bilimi ve Mühendisliği, *Mater. Sci. Eng.*, 2014, **20**, p 103.
18. M. Ghaffari, A. Vahedi Nemani, M. Rafieezad, and A. Nasiri, Effect of Solidification Defects and HAZ Softening on the Anisotropic Mechanical Properties of a Wire Arc Additive-Manufactured Low-Carbon Low-Alloy Steel Part, *JOM*, 2019, **71**, p 4215–4224. <https://doi.org/10.1007/s11837-019-03773-5>
19. M. Rafieezad, M. Ghaffari, A. Vahedi Nemani, and A. Nasiri, Microstructural Evolution and Mechanical Properties of a loW-Carbon Low-Alloy Steel Produced by Wire Arc Additive Manufacturing, *Int J Adv Manuf Technol*, 2019, **105**, p 2121–2134. <https://doi.org/10.1007/s00170-019-04393-8>
20. E. Aldalur, F. Veiga, A. Suárez, J. Bilbao, and A. Lamikiz, High Deposition Wire Arc Additive Manufacturing of Mild Steel: Strategies and Heat Input Effect on Microstructure and Mechanical Properties, *J. Manuf. Process.*, 2020, **58**, p 615–626. <https://doi.org/10.1016/j.jmapro.2020.08.060>
21. C.V. Haden, G. Zeng, F.M. Carter, C. Ruhl, B.A. Krick, and D.G. Harlow, Wire and Arc Additive Manufactured Steel: Tensile and Wear Properties, *Addit. Manuf.*, 2017, **16**, p 115–123. <https://doi.org/10.1016/j.addma.2017.05.010>
22. J.V. Gordon, C.V. Haden, H.F. Nied, R.P. Vinci, and D.G. Harlow, Fatigue Crack Growth Anisotropy, Texture and Residual Stress in Austenitic Steel Made by Wire and Arc Additive Manufacturing, *Mater. Sci. Eng. A*, 2018, **724**, p 431–438. <https://doi.org/10.1016/j.msea.2018.03.075>
23. D. Yang, H. Fang, Y. Peng, J. Fan, Y. Huang, K. Wang et al., Investigation of Spatters in Cold Metal Transfer+Pulse-Based Wire and Arc Additive Manufacturing of High Nitrogen Austenitic Stainless Steel, *J. Mater. Eng. Perform.*, 2021, **30**, p 6881–6894. <https://doi.org/10.1007/s11665-021-06048-w>
24. X. Zhang, Q. Zhou, K. Wang, Y. Peng, J. Ding, J. Kong et al., Study on Microstructure and Tensile Properties of High Nitrogen Cr-Mn Steel PROCESSED by CMT Wire and Arc Additive Manufacturing, *Mater. Des.*, 2019, **166**, p 107611. <https://doi.org/10.1016/j.matdes.2019.107611>
25. D. Yang, Y. Huang, J. Fan, M. Jin, Y. Peng, and K. Wang, Effect of N₂ Content in Shielding Gas on Formation Quality and Microstructure of High Nitrogen Austenitic Stainless Steel Fabricated by Wire and Arc Additive Manufacturing, *J. Manuf. Process.*, 2021, **61**, p 261–269. <https://doi.org/10.1016/j.jmapro.2020.11.020>
26. P. Dirisu, G. Supriyo, F. Martina, X. Xu, and S. Williams, Wire Plus Arc Additive Manufactured Functional Steel Surfaces Enhanced by Rolling, *Int. J. Fatigue.*, 2020, **130**, p 105237. <https://doi.org/10.1016/j.ijfatigue.2019.105237>
27. H. Bartsch, R. Kühne, S. Citarelli, S. Schaffrath, and M. Feldmann, Fatigue Analysis of Wire arc Additive Manufactured (3D Printed) Components with Unmilled Surface, *Structures*, 2021, **31**, p 576–589. <https://doi.org/10.1016/j.istruc.2021.01.068>
28. T. Ron, G.K. Levy, O. Dolev, A. Leon, A. Shirizly, and E. Aghion, The Effect of Microstructural Imperfections on Corrosion Fatigue of Additively Manufactured ER70S-6 Alloy Produced by Wire Arc Deposition, *Metals*, 2020, **10**, p 98. <https://doi.org/10.3390/met10010098>
29. B. Guennec, A. Ueno, T. Sakai, M. Takanashi, and Y. Itabashi, Effect of the Loading Frequency on Fatigue Properties of JIS S15C Low Carbon Steel and Some Discussions Based on Micro-Plasticity Behavior, *Int. J. Fatigue*, 2014, **66**, p 29–38. <https://doi.org/10.1016/j.ijfatigue.2014.03.005>
30. A.A. Zainulabdeen, Study of Fatigue Fractography of Mild Steel Used in Automotive Industry, *Alkej.*, 2019, **15**, p 82–8. <https://doi.org/10.22153/kej.2019.07.003>
31. T. Abe and H. Sasahara, Dissimilar Metal Deposition with a Stainless Steel and Nickel-based Alloy Using Wire and Arc-based Additive Manufacturing, *Precis. Eng.*, 2016, **45**, p 387–395. <https://doi.org/10.1016/j.precisioneng.2016.03.016>
32. L. Lu, Y. Tian, Y. Cai, Y. Xin, X. Chen, and G. Zhang et al., Microstructure and Mechanical Properties of a Functionally Graded Material from TA1 to Inconel 625 Fabricated by Dual Wire + Arc Additive Manufacturing, *Mater. Lett.*, 2021, **298**, p 130010. <https://doi.org/10.1016/j.matlet.2021.130010>
33. P. Sędek, J. Brózda, L. Wang, and P.J. Withers, Residual Stress Relief in MAG Welded Joints of Dissimilar Steels, *Int. J. Press. Vessels Pip.*, 2003, **80**, p 705–713. <https://doi.org/10.1016/j.ijpvp.2003.08.004>

Publisher's Note Springer Nature remains neutral with regard to jurisdictional claims in published maps and institutional affiliations.

Springer Nature or its licensor (e.g. a society or other partner) holds exclusive rights to this article under a publishing agreement with the author(s) or other rightsholder(s); author self-archiving of the accepted manuscript version of this article is solely governed by the terms of such publishing agreement and applicable law.